One-Dimensional Poole-Frenkel Conduction in the Single Defect Limit

4 AUTHORS, INCLUDING:

Elliot Fuller
Sandia National Laboratories
7 PUBLICATIONS **14** CITATIONS

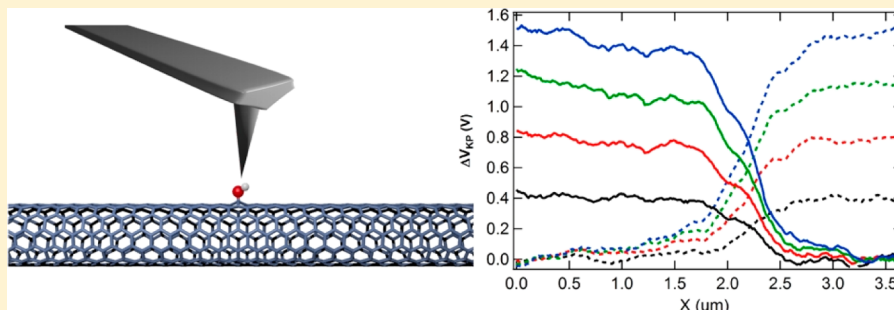SEE PROFILE

O. Tolga Gul
Gazi University
21 PUBLICATIONS **56** CITATIONS

SEE PROFILE

One-Dimensional Poole-Frenkel Conduction in the Single Defect Limit

Deng Pan,[†] Elliot J. Fuller,[†] O. Tolga Gül, and Philip G. Collins[*]

Department of Physics and Astronomy, University of California at Irvine, Irvine, California 92697, United States

ABSTRACT: A single point defect surrounded on either side by quasi-ballistic, semimetallic carbon nanotube is a nearly ideal system for investigating disorder in one-dimensional (1D) conductors and comparing experiment to theory. Here, individual single-walled nanotubes (SWNTs) are investigated before and after the incorporation of single point defects. Transport and local Kelvin Probe force microscopy independently demonstrate high-resistance depletion regions over 1.0 μm wide surrounding one point defect in semimetallic SWNTs. Transport measurements show that conductance through such wide depletion regions occurs via a modified, 1D version of Poole—Frenkel field-assisted emission. Given the breadth of theory dedicated to the possible effects of disorder in 1D systems, it is surprising that a Poole-Frenkel mechanism appears to describe defect scattering and resistance in this semimetallic system.

KEYWORDS: Carbon nanotube, Kelvin probe force microscopy, defect scattering, point defect

A single point defect can convert a ballistic, one-dimensional (1D) conductor into a more resistive wire,[1−5] and a pair of defects can produce Coulomb blockade effects as high as room temperature.[6] Driven by these dramatic effects, the current International Technology Roadmap for Semiconductors[7] calls for physics models to better address the role of single defects and dopants in semiclassical 1D devices. Unfortunately, well-characterized systems for studying defect-induced effects is acknowledged as a challenging gap to address experimentally.[8] Theory predicts a range of novel quantum phenomena with practical consequences in disordered 1D conductors,[9−16] such as resistivity dipoles and Luttinger scaling exponents. However, experiments are often limited to random contaminants and imperfections of unknown character. The precision placement of individual atoms into conducting structures, either using scanning probe tips[17] or by implantation,[5,18] is a notable example for which quantum transport has been studied at cryogenic temperatures, but these quantum states are not robust at higher temperatures.

On the other hand, single-walled carbon nanotubes (SWNTs) exhibit a quantum-mechanical regime extending to room temperature[19] with hints of Luttinger liquid behaviors above 100 K.[19−21] In past work, SWNTs have been a poor example of precision control: disorder in SWNTs has been ubiquitous, random, and varied.[1−3,22,23] Recently, we demonstrated an electrochemical technique for adding a single oxidative adduct to SWNT transistor devices.[24] These oxidized

defect sites were sufficiently disruptive to affect SWNT conductance at room temperature and in relatively "clean" SWNT devices (those exhibiting room-temperature inelastic mean free paths >1 μm), they could be the sole inelastic scattering site. Here, we report measurements comparing individual SWNTs before and after defect incorporation and show that these sites fail to demonstrate the power-law scaling of a Luttinger liquid or the activated thermodynamics of a simple barrier. Instead, defect scattering in SWNTs has the temperature and bias dependence of Poole—Frenkel conduction, though with modifications accounting for the 1D electrostatics. The Poole—Frenkel mechanism,[25,26] which is frequently applied to thin, 2D insulators,[27] has never been observed in the limit of a single defect, and its applicability to point defect scattering in a 1D channel is wholly unanticipated in the theoretical literature. Some past research has reported Poole-Frenkel conduction in SWNTs,[28−34] but it has always been attributed to ensemble disorder.

Experimental Methods. To accomplish this work, devices containing isolated SWNTs were prepared using techniques typical for this field.[24] SWNTs were grown on 4″ p++ Si wafers having a 300 nm, thermally grown oxide by catalyst-assisted

chemical vapor deposition (CVD).[24,35] CVD used extremely dilute catalyst coverage to create well-separated SWNTs having diameters of 0.9 to 1.7 nm, as verified individually by atomic force microscopy (AFM). Ti or Pt/Ti electrodes were patterned onto the randomly grown SWNTs using optical lithography. Electrode spacings of 2 μm, combined with the various angles of intersection with SWNTs, gave channel lengths ranging from 2 to 6 μm. Figure 1a depicts a schematic
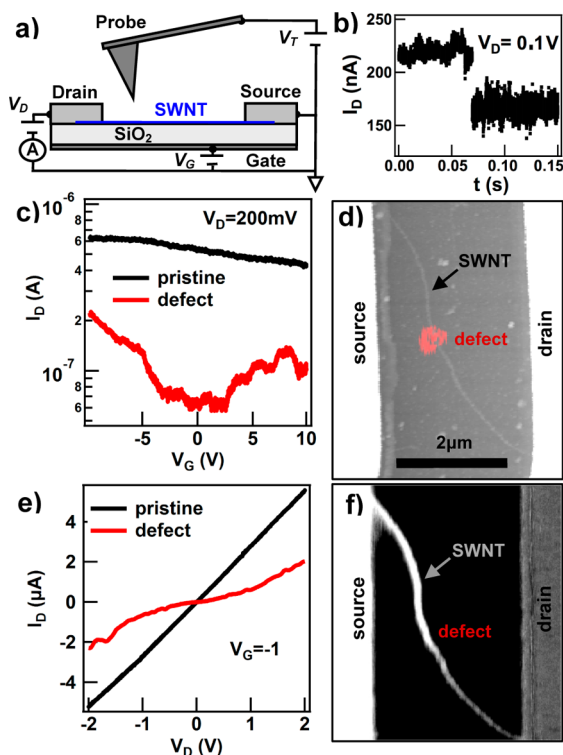
Figure 1. Carbon nanotubes with single point defects. (a) Three-terminal and scanning probe characterization of a m-SWNT. (b) Example drop in I_D used to identify point-defect incorporation by electrochemical oxidation. (c) $I_D(V_G)$ before and after defect incorporation with (d) SGM image of the localized nature of the new gate dependence. (e) $I_D(V_D)$ at $V_G = -1$ V before and after defect incorporation, and (f) corresponding KPFM image illustrating the large potential gradient at the same site. All data acquired at $T = 180$ K.

of the device layout, with the p++ Si serving as a back gate electrode. Electronic characterization of the source-drain current (I_D) as a function of drain and gate biases (V_D and V_G) identified quasi-metallic samples (m-SWNTs) with modest V_G sensitivity that were the primary focus of this investigation.

Single point defects were introduced into each SWNT using the method of conductance-controlled point functionalization.[24,36] Briefly, this method uses $I_D(t)$ as a real-time indicator of covalent modifications during the dilute electrochemical oxidation of a SWNT device.[24,28] SWNT channels were covered with a water droplet, and then $I_D(t)$ was monitored while the potential of the SWNT was slowly raised above the threshold for electrochemical oxidation by water, which was typically 0.9−1.1 V. At this threshold, individual oxidation events occur stochastically with waiting times of seconds. The oxidation, which is believed to be the covalent addition of an −OH adduct, was precisely limited to a single stepped drop in $I_D(t)$ defect using a software trigger with a 30 ms response time

that dropped the oxidative potential down to 0 V. In this manner, single defects were achieved in 80% of attempts and further oxidative damage was strictly limited. Figure 1b shows a typical $I_D(t)$ trace in which a device increased resistance from 430 to 600 kΩ in one discrete step while being held at 1.0 V. Oxidation occurred at a random position along each SWNT channel, and then the sites were subsequently located by scanning-probe imaging.[24]

To precisely determine the electronic effects of a defect, each SWNT was characterized before and after this electrochemical defect incorporation. After oxidation, devices were immediately blown dry and transferred into a high-vacuum (10^{-7} Torr), variable-temperature transport and AFM system (JEOL JSPM 5200) that was used to acquire $I_D(V_D,V_G,T)$ and surface maps of local properties. Frequency-modulated Kelvin probe force microscopy (KPFM) was used to image surface potentials V_{KP} and potential gradients resulting from scattering.[37] using a custom-designed KPFM system that has been described previously.[38,39] Scanning gate microscopy (SGM) was also used to locate the defects based on their localized gate sensitivity dI/dV_G.[40−42] Images shown here were all acquired at 185 K to eliminate hysteresis and drift associated with mobile surface contaminants at higher temperatures. In our system, custom electronics synchronized AFM imaging to the acquisition of I_D and control of V_D, V_G, and the probe tip potential V_T. In this work, the lateral KPFM resolution was limited to 10−50 nm by the probe geometry.[38] This resolution was at least ten times narrower than the average potential gradients analyzed below, so tip resolution does not affect the conclusions drawn.

Results. Figure 1 illustrates the increases of resistance and gate sensitivity that accompanied the addition of a defect to an example m-SWNT. Compared to the pristine case before modification, the damaged m-SWNT exhibited a higher low-bias resistance, a non-Ohmic $I_D(V_D)$, and twice as much gate modulation in $I_D(V_G)$ (Figure 1c,e), all in accord with previous reports.[24,43] Scanning probe imaging further proved these effects to be localized. Figure 1d shows an SGM image of dI_D/dV_G (red) overlaid on AFM topography (gray), indicating how the increased gate sensitivity in Figure 1c was entirely concentrated at one spot midway between the source and drain connections. Figure 1f shows that KPFM imaging of V_{KP} under similar conditions ($V_G = -1$ V) resolved a large potential drop at the same location. In comparison, pristine m-SWNTs exhibited shallow KPFM potential gradients with large drops at the electrode interfaces[38,39] and minimal SGM sensitivity.[41,43] Data from other SWNTs showed qualitatively similar features to Figure 1. Semiconducting SWNTs, which have intrinsic gate responses and Schottky barrier effects,[37,40,44] have been excluded from this report in favor of the simpler characteristics of m-SWNTs, which are more straightforward to interpret.

Two experimental methods were used to investigate the added resistance associated with point defects. Higher-resolution KPFM versus V_D and I_D allowed for a detailed investigation of the potential gradients surrounding a scattering site. Figure 2a shows a set of KPFM images acquired from the device of Figure 1 as it was biased from +2.0 to −2.0 V in 0.5 V increments (from left to right, with $V_D = 0$ not shown).[45] These images have been cropped to highlight the region surrounding the SWNT defect and line cuts along the SWNT channel (Figure 2b) were extracted for analysis. At the locus of SGM sensitivity, KPFM resolved a small potential barrier at $V_D = 0$ (Figure 2b, bottom) and a symmetric, high-field potential drop
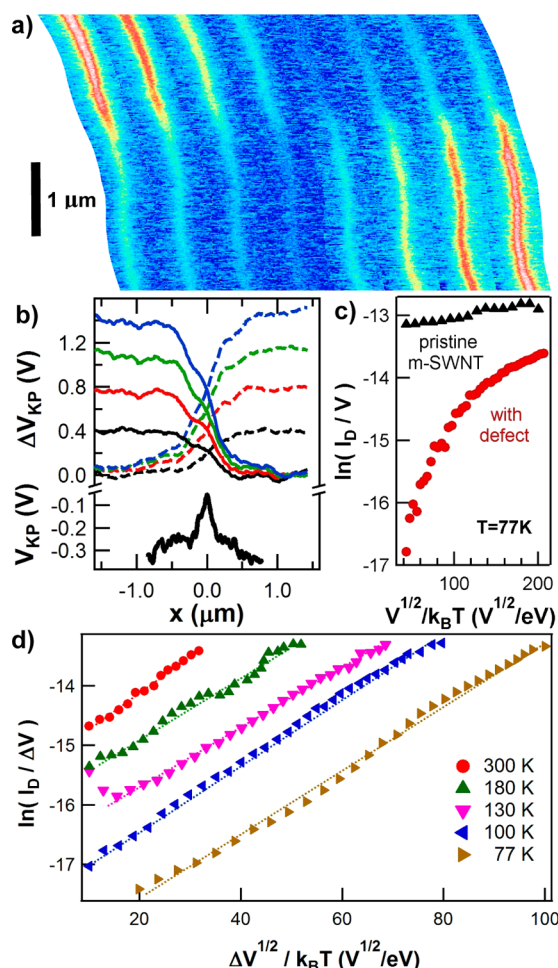
Figure 2. Potential gradients around defect sites. (a) Selected portions of KPFM images around a m-SWNT defect site at V_D = +2 to −2 V in 0.5 V steps. (b) KPFM line cuts extracted along the m-SWNT, with reverse-bias data plotted as dashed lines. (c) Example Poole−Frenkel plots of raw data $I_D(V_D)$ at T = 77 K before and after defect incorporation. (d) Poole−Frenkel plot of the differential, added resistance $I_D(\Delta V_D, T)$ with fits to eq 1 (dashed lines).

$F = dV_{KP}/dx$ in response to currents (Figure 2b, top). For example, at V_D = 1 V the KPFM potential drop ΔV_{KP} was 0.68 ± 0.04 V and the field reached F = 0.76 V/μm. This drop in potential corresponded to a local resistance $\Delta V_{KP}/I_D$ = 928 ± 54 kΩ that was two-thirds of the total device resistance and that matched the two-terminal increase measured at the same temperature and bias. In this manner, KPFM allowed direct measurements of each defect's resistance, independent of contact resistances and diffusive scattering along the rest of the SWNT. Diffusive scattering far from defect sites has been extensively investigated at low and high bias by transport techniques[46−48] and by quantitative KPFM,[38,39] so it is not the focus of this report.

To complement direct KPFM imaging, two-terminal measurements of $I_D(V_D, V_G, T)$ were acquired over a wider range of bias and temperature. Figure 2c shows an example measurement of $I_D(V_D)$ at T = 77 K plotted on axes used for Poole−Frenkel (PF) analysis. The pristine SWNT had an ohmic, temperature-independent conductance that resulted in a nearly horizontal line on these axes; the addition of a defect reduced the conductance and induced a nonohmic bias dependence. The PF axes are clearly inappropriate for the

raw data, which unlike KPFM include the contact resistance and diffusive channel contributions. However, careful subtraction of $I_D(V_D)$ data sets before and after defect incorporation allowed us to define the additional drain voltage ΔV_D necessary to obtain a particular current I_D at fixed V_G and T. This subtraction approximates the semiclassical limit of the Landauer−Buttiker formalism in which each constituent scattering mechanism constitutes a series resistance. So long as point functionalization occurs far from the electrodes and does not affect the SWNT's contact resistance or inelastic mean free path, the addition of one new scattering site introduces an extra voltage drop ΔV_D for a given I_D. A similar distinction between $I_D(V_D)$ and $I_D(\Delta V_D)$ can be used to analyze ensemble radiation damage.[49]

Discussion. The $I_D(\Delta V_D)$ difference curves suggested bias increases ΔV_D that were in excellent agreement with the potential drops ΔV_{KP} measured directly by KPFM. Furthermore, these curves fit the functional form of Poole−Frenkel (PF) conduction over a wide range of bias and temperature. PF conduction is governed by

$$I_D(\Delta V_D, T) = a\Delta V_D \exp\left[\frac{-q(\Phi_0 - bF^{1/2})}{k_B T}\right] \quad (1)$$

where the detrapping electric field F is proportional to ΔV_D and a and b are both positive constants.[26,50] PF fitting for $I_D(\Delta V_D)$ curves at six temperatures is shown in Figure 2d. Plots of $\ln(I_D/\Delta V_D)$ versus $\Delta V_D^{1/2}/T$ at different temperatures produced a family of nearly parallel, straight-line curves for each m-SWNT we have investigated.

The PF model is most frequently used to understand the transport that occurs when localized defect states enhance conduction through thin, insulating films.[27,50] The unbiased and biased situations are depicted by energy diagrams in Figure 3a. Each defect is modeled as a Coulomb trap with a barrier Φ_o in an insulating film of thickness D and dielectric constant ε. When the insulator is biased, charges may tunnel into this trapping state and then be emitted into the insulator's conduction band. The PF mechanism describes the following emission: the mean applied field $F = \Delta V_D/\varepsilon D$ lowers the
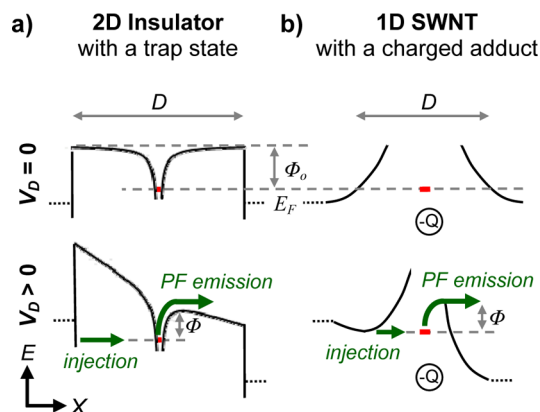
Figure 3. Energy band diagrams compare conventional Poole−Frenkel conduction through a 2D insulator and through the depletion region surrounding a SWNT defect. In both cases, the insulating region has a characteristic dimension D, a defect-induced trap state (red), and an effective barrier height $\Phi < \Phi_o$. Φ is on the order of 1 eV for a conventional insulator but only 10−50 meV for the small band gap of a m-SWNT. E_F is the Fermi energy of carriers.

barrier from Φ_o to Φ by an amount proportional to $F^{1/2}$,[26,51] leading to the functional form expressed in eq 1. PF plots like the one shown in Figure 2d can be used to extract experimental values of Φ_o,[51,52] which are typically 1−2 eV for traps in SiO_2.

Fitting eq 1 to SWNT data results in inferred barrier heights Φ_o of only 10−40 meV and small detrapping fields F, the latter of which suggest effective lengths $D = \Delta V_D / \varepsilon F$ approaching the 2 μm source-drain separation. Such small barriers and wide lengths were discounted as unphysical in the first report of PF conduction in SWNTs[28] but subsequent researchers have repeatedly shown that highly disordered and damaged SWNT films can all be fit to eq 1.[29−34] The application of eq 1 to point disorder in 1D m-SWNTs is not self-evident because the electrostatics of the PF mechanism across 2D insulators and 1D conductors are so dissimilar. Furthermore, detrapping fields F over micron-scale lengths seem inconsistent with the single-defect limit studied here. In 2D insulating films, the PF mechanism can be relevant for insulators up to 300 nm thick, but only because the model can be extended to ensembles of traps having broad energy distributions.[51,52]

Nevertheless, KPFM imaging directly observes fields on the order of 1 V/μm and potentials ΔV_D dropping over micrometer distances, proving that the lengths inferred from PF fitting are physically relevant. As one example, the PF slopes in Figure 2d were observed in KPFM as a high-F region extending for 0.9 ± 0.1 μm. As seen in Figure 2b, the width of the high-F region was relatively insensitive to V_D and it extended symmetrically around the defect site. Similar agreement between KPFM and transport has been observed in all SWNT samples, proving that eq 1 appropriately captures the bias dependence for single-defect scattering in a SWNT. Furthermore, PF fitting to eq 1 determines the average field $\Delta V_D / \varepsilon D$ and KPFM measurements observe ΔV_D and D, so the two can be combined to solve for ε. The resulting value of approximately 2.5 is intermediate between air and SiO_2, as is generally assumed for exposed SWNT devices. Previously, authors reporting PF fitting have hypothesized that small fields F were evidence of diffusive scattering due to gross disorder introduced by SWNT processing, entanglement, or other materials issues.[29−34] Here, before-and-after imaging in the single-defect limit proves that F is small because ΔV_D drops uniformly over substantial widths.

Moreover, experimental agreement between transport and KPFM also covered the strong gate sensitivity shown in Figure 1c. Transport data for different m-SWNTs led to detailed sets of $I_D(\Delta V_D, V_G, T)$ data, each of which exhibited excellent fits to eq 1 ($0.9 < R < 1$) when the two parameters $\Phi_o(V_G)$ and $D(V_G)$ were allowed to be gate-dependent. Figure 4a shows $D(V_G)$ and $\Phi_o(V_G)$ from one m-SWNT with ±1σ error bars to illustrate which features were significant (and assuming a value ε = 2.5 intermediate between SiO_2 and air). Ignoring fine details, similar features across different devices included sharp extrema, broad regions insensitive to V_G, and anticorrelated Φ_o and D. KPFM was too laborious to map the full V_G dependence but it was used to confirm that high-F regions widened or shortened in response to moderate gating at V_G = −1, 0, and +1 V. This direct imaging helped prove that the width of high-F regions like those shown in Figure 2b were much more sensitive to V_G than to V_D. KPFM also revealed that SWNT diameter played an important role in systematically scaling with width of the high-F regions, which ranged from 0.3 to 0.9 μm for one m-SWNT but from 1.1 to 2.4 μm for another. Figure 4b shows KPFM measurements of this apparent width at V_G = −1
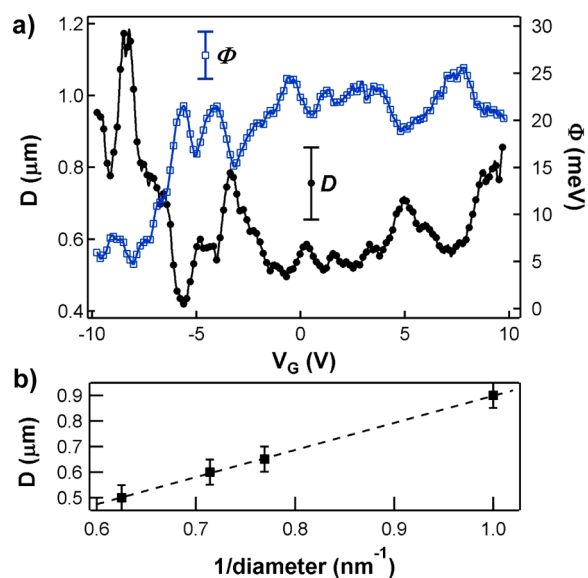
Figure 4. (a) Gate dependence of defect-induced barrier width D and height Φ in a 1.6 nm m-SWNT. (b) Comparison of D among four m-SWNTs, all measured at V_G = −1 V and confirmed by direct KPFM imaging. Dashed line shows least-squares fit to an inverse diameter law. All error bars are one standard deviation.

V from four m-SWNTs with a fit illustrating the inverse diameter dependence $D = (1.06 \pm 0.01\ nm)(\text{diameter})^{-1}$. Variability in extrinsic doping among different SWNTs limited a more quantitative comparison, but future work could investigate gate dependence in more detail.

Finally, we note that the applicability of eq 1 was surprisingly insensitive to the extent of chemical disorder. Point-function-alized devices having very modest (∼10%) increases in room temperature resistance were compared against devices that had been exposed to more extensive electrochemical oxidation, ultimately up to the limit of near-insulating devices analyzed previously.[24,28−34] When the differential technique described above was used to isolate ΔV_D and analyze only the increase in resistance, all types of damage exhibited a PF bias dependence with apparent barriers a few tens of millielectronvolts high and widths of 0.3 μm or more.

The results described here challenge conventional theoretical treatments of SWNT defect scattering, which have not previously predicted a PF bias dependence or micrometer-scale high-field regions. We believe the most relevant work is the prediction that point charges near a SWNT can induce carrier depletion over widths exceeding 1 μm.[53,54] The Coulomb potential of a charged adduct, such as the −OH chemical group introduced here, is essentially unscreened by the small, 1D carrier density of m-SWNTs. At V_D = 0, KPFM around defects directly imaged sharp potential peaks on top of broad shoulders, and we interpret these features as charged defects surrounded by zones of carrier depletion (Figure 2b). At $V_D > 0$, the depletion zones result in high-field regions that stay symmetrically centered around the defect but which vastly exceed the defect's spatial extent. In fact, such long depletion widths appear to be a hallmark of SWNT conduction. At Schottky barrier interfaces, Freitag et al. used scanning photovoltage imaging to image band bending and depletion widths extending over many microns.[55] SWNT screening lengths are predicted to depend sensitively on SWNT diameter, chirality, and carrier density with a general trend toward better

screening in larger diameter SWNTs[56,57] due to weaker charge confinement effects.[53,54] All of these elements are supported by observations described here, though we do not rule out other possible phenomena such as negative quantum capacitance.[58,59]

The applicability of eq 1 further requires that field-assisted emission from localized states is a key to the conduction observed through these wide depletion regions. A charged adduct and its associated disorder have one or more localized electronic states that may be involved, and we propose that trapping and detrapping by this state is responsible for the successful fitting to eq 1. Figure 3 illustrates the functional equivalency between the conventional, 2D insulator having a charged trap state (Figure 3a) and the depleted region of a 1D m-SWNT surrounding a charged adduct (Figure 3b). The band bending and depletion in the m-SWNT that are observed by KPFM at zero bias produce a semi-insulating region that plays a role similar to the insulating film; at high field, charge injection into the SWNT defect state and field-induced emission out of it lead to conduction that mimics the PF behavior of thin films. In addition, the high fields and disorder may hybridize the SWNT subbands or allow mechanisms such as interband Zener tunneling[60] to introduce the necessary states. We note that Φ_o is comparable to the small band gaps of m-SWNTs[19] and that any model of hybridized m-SWNT subbands would symmetrically accommodate defects having either positive or negative charge. In any case, first-principles modeling will be needed to determine the exact mechanisms that allow eq 1 to apply to defect scattering in SWNTs. The conventional interpretation in PF conduction has no explicit dependence on carrier density nor V_G, because neither of these has a role in determining F in 2D insulating thin films. Furthermore, trap emission depends exponentially on F, which in 1D has unique electrostatics and is sensitive to details of the carrier concentration, confinement effects, and electron correlation.[61,62]

Conclusion. In conclusion, we directly imaged potential drops surrounding single, isolated SWNT defects and found that the high-field regions could extend to over 1 μm in length, which is in agreement with theoretical predictions of divergent depletion lengths in 1D.[53] Conduction through these depletion regions followed a gate-dependent, Poole−Frenkel-like characteristic that challenges existing models of defect resistance. Such long depletion lengths have not been reported in PF-limited semiconductor nanowires[54,63] or 2D graphene in the low-carrier density limit.[64,65] As emphasized by Yu et al.,[64] the combination of low carrier densities and a 1D geometry may prove to be critical for understanding not only the effects of defects and disorder but also heterojunctions and contact resistance in extremely scaled semiconductor devices.

■ AUTHOR INFORMATION

Corresponding Author
*E-mail: collinsp@uci.edu.

Author Contributions
[†]D.P. and E.J.F. contributed equally to this work.

Notes
The authors declare no competing financial interest.

■ REFERENCES

(1) Bockrath, M.; Liang, W. J.; Bozovic, D.; Hafner, J. H.; Lieber, C. M.; Tinkham, M.; Park, H. *Science* **2001**, *291*, 283.

(2) Freitag, M.; Johnson, A. T.; Kalinin, S. V.; Bonnell, D. A. *Phys. Rev. Lett.* **2002**, *89*, 216801.

(3) Kalinin, S. V.; Bonnell, D. A.; Freitag, M.; Johnson, A. T. *Appl. Phys. Lett.* **2002**, *81*, 5219.

(4) Auslaender, O. M.; Yacoby, A.; de Picciotto, R.; Baldwin, K. W.; Pfeiffer, L. N.; West, K. W. *Science* **2002**, *295*, 825.

(5) Tan, K. Y.; Chan, K. W.; Möttönen, M.; Morello, A.; Yang, C.; Donkelaar, J. v.; Alves, A.; Pirkkalainen, J.-M.; Jamieson, D. N.; Clark, R. G.; Dzurak, A. S. *Nano Lett.* **2010**, *10*, 11.

(6) Postma, H. W. C.; Teepen, T.; Yao, Z.; Grifoni, M.; Dekker, C. *Science* **2001**, *293*, 76.

(7) Cogez, P.; Graef, M.; Huizing, B.; Mahnkopf, R.; Ishiuchi, H.; Ikumi, N.; Choi, S.; Choi, J. H.; Diaz, C. H.; See, Y. C.; Gargini, P.; Kingscott, T.; Steff, I. *The International Technology Roadmap for Semiconductors*; Sematech: Albany, New York, 2013.

(8) Koenraad, P. M.; Flatte, M. E. *Nat. Mater.* **2011**, *10*, 91.

(9) Landauer, R. Z. *Phys. B: Condens. Matter Quanta* **1975**, *21*, 247.

(10) Sorbello, R. S. *Phys. Rev. B: Condens. Matter Mater. Phys.* **1981**, *23*, 5119.

(11) Glazman, L. I.; Ruzin, I. M.; Shklovskii, B. I. *Phys. Rev. B: Condens. Matter Mater. Phys.* **1992**, *45*, 8454.

(12) Voit, J. *Rep. Prog. Phys.* **1995**, *58*, 977.

(13) Egger, R.; Grabert, H. *Phys. Rev. Lett.* **1995**, *75*, 3505.

(14) Egger, R.; Grabert, H. *Phys. Rev. Lett.* **1996**, *77*, 538.

(15) Hugle, S.; Egger, R. *Europhys. Lett.* **2004**, *66*, 565.

(16) Asenov, A.; Brown, A. R.; Davies, J. H.; Kaya, S.; Slavcheva, G. *IEEE Trans. Electron Devices* **2003**, *50*, 1837.

(17) Fuechsle, M.; Miwa, J. A.; Mahapatra, S.; Ryu, H.; Lee, S.; Warschkow, O.; Hollenberg, L. C. L.; Klimeck, G.; Simmons, M. Y. *Nat. Nanotechnol.* **2012**, *7*, 242.

(18) Shinada, T.; Okamoto, S.; Kobayashi, T.; Ohdomari, I. *Nature* **2005**, *437*, 1128.

(19) Deshpande, V. V.; Bockrath, M.; Glazman, L. I.; Yacoby, A. *Nature* **2010**, *464*, 209.

(20) Bockrath, M.; Cobden, D. H.; Lu, J.; Rinzler, A. G.; Smalley, R. E.; Balents, T.; McEuen, P. L. *Nature* **1999**, *397*, 598.

(21) Ishii, H.; Kataura, H.; Shiozawa, H.; Yoshioka, H.; Otsubo, H.; Takayama, Y.; Miyahara, T.; Suzuki, S.; Achiba, Y.; Nakatake, M.; Narimura, T.; Higashiguchi, M.; Shimada, K.; Namatame, H.; Taniguchi, M. *Nature* **2003**, *426*, 540.

(22) Bachtold, A.; Fuhrer, M. S.; Plyasunov, S.; Forero, M.; Anderson, E. H.; Zettl, A.; McEuen, P. L. *Phys. Rev. Lett.* **2000**, *84*, 6082.

(23) Woodside, M. T.; McEuen, P. L. *Science* **2002**, *296*, 1098.

(24) Goldsmith, B. R.; Coroneus, J. G.; Khalap, V. R.; Kane, A. A.; Weiss, G. A.; Collins, P. G. *Science* **2007**, *315*, 77.

(25) Frenkel, J. *Phys. Rev.* **1938**, *54*, 647.

(26) Simmons, J. G. *Phys. Rev.* **1967**, *155*, 657.

(27) Simmons, J. G. *J. Phys. D: Appl. Phys.* **1971**, *4*, 613.

(28) Mannik, J.; Goldsmith, B. R.; Kane, A.; Collins, P. G. *Phys. Rev. Lett.* **2006**, *97*, 16601.

(29) Jombert, A. S.; Coleman, K. S.; Wood, D.; Petty, M. C.; Zeze, D. A. *J. Appl. Phys.* **2008**, *104*, 094503.

(30) Mabrook, M. F.; Pearson, C.; Jombert, A. S.; Zeze, D. A.; Petty, M. C. *Carbon* **2009**, *47*, 752.

(31) Perello, D. J.; Yu, W. J.; Bae, D. J.; Chae, S. J.; Kim, M. J.; Lee, Y. H.; Yun, M. *J. Appl. Phys.* **2009**, *105*, 124309.

(32) Perello, D. J.; Bae, D. J.; Kim, M. J.; Cha, D.; Jeong, S. Y.; Kang, B. R.; Yu, W. J.; Lee, Y. H.; Yun, M. *IEEE Trans. Nanotechnol.* **2009**, *8*, 355.

(33) Salehi-Khojin, A.; Field, C. R.; Yeom, J.; Masel, R. I. *Appl. Phys. Lett.* **2010**, *96*, 163110.

(34) Salehi-Khojin, A.; Lin, K. Y.; Field, C. R.; Masel, R. I. *Science* **2010**, *329*, 1327.

(35) An, L.; Owens, J. M.; McNeil, L. E.; Liu, J. *J. Am. Chem. Soc.* **2002**, *124*, 13688.

(36) Coroneus, J. G.; Goldsmith, B. R.; Lamboy, J. A.; Kane, A. A.; Collins, P. G.; Weiss, G. A. *ChemPhysChem* **2008**, *9*, 1053.

(37) Miyato, Y.; Kobayashi, K.; Matsushige, K.; Yamada, H. *Jpn. J. Appl. Phys.* **2010**, *49*, 49.

(38) Fuller, E. J.; Pan, D.; Corso, B. L.; Gul, O. T.; Gomez, J. R.; Collins, P. G. *Appl. Phys. Lett.* **2013**, *102*, 083503.

(39) Fuller, E. J.; Pan, D.; Corso, B. L.; Gul, O. T.; Collins, P. G. *Phys. Rev. B: Condens. Matter Mater. Phys.* **2014**, *89*, 245450.

(40) Staii, C.; Johnson, A. T.; Shao, R.; Bonnell, D. A. *Nano Lett.* **2005**, *5*, 893.

(41) Hunt, S. R.; Wan, D.; Khalap, V. R.; Corso, B. L.; Collins, P. G. *Nano Lett.* **2011**, *11*, 1055.

(42) Hunt, S. R.; Fuller, E. J.; Corso, B. L.; Collins, P. G. *Phys. Rev. B: Condens. Matter Mater. Phys.* **2012**, *85*, 235418.

(43) Fan, Y.; Goldsmith, B. R.; Collins, P. G. *Nat. Mater.* **2005**, *4*, 906.

(44) Miyato, Y.; Kobayashi, K.; Matsushige, K.; Yamada, H. *Jpn. J. Appl. Phys.* **2005**, *44*, 1633.

(45) Exchanging the role of source and drain produced the most intuitive and directly comparable images of reverse polarity, so that technique has been used here.

(46) Yao, Z.; Dekker, C.; Avouris, P. Electrical transport through single-wall carbon nanotubes. In *Carbon Nanotubes*; Dresselhaus, M. S., Dresselhaus, G., Avouris, P., Eds.; Springer: New York, **2001**; Vol. *80*, p 147.

(47) Freitag, M.; Tsang, J. C.; Bol, A.; Avouris, P.; Yuan, D. N.; Liu, J. *Appl. Phys. Lett.* **2007**, *91*, 031101.

(48) Chandra, B.; Perebeinos, V.; Berciaud, S.; Katoch, J.; Ishigami, M.; Kim, P.; Heinz, T. F.; Hone, J. *Phys. Rev. Lett.* **2011**, *107*, 146601.

(49) Srour, J. R.; Marshall, C. J.; Marshall, P. W. *IEEE Trans. Nucl. Sci.* **2003**, *50*, 653.

(50) Sze, S. M. *Physics of Semiconductor Devices*, 2nd ed.; John Wiley & Sons: New York, 1981; p 868.

(51) Specht, M.; Stadele, M.; Jakschik, S.; Schroder, U. *Appl. Phys. Lett.* **2004**, *84*, 3076.

(52) Yeargan, J. R.; Taylor, H. L. *J. Appl. Phys.* **1968**, *39*, 5600.

(53) Leonard, F.; Tersoff, J. *Phys. Rev. Lett.* **1999**, *83*, 5174.

(54) Leonard, F.; Talin, A. A. *Nat. Nanotechnol.* **2011**, *6*, 773.

(55) Freitag, M.; Tsang, J. C.; Bol, A.; Yuan, D. N.; Liu, J.; Avouris, P. *Nano Lett.* **2007**, *7*, 2037.

(56) Liang, G. C.; Ghosh, A. W.; Paulsson, M.; Datta, S. *Phys. Rev. B: Condens. Matter Mater. Phys.* **2004**, *69*, 115302.

(57) Datta, S. *Electronic Transport in Mesoscopic Systems*; Cambridge University Press: Cambridge, 1995.

(58) Latessa, L.; Pecchia, A.; Di Carlo, A.; Lugli, P. *Phys. Rev. B: Condens. Matter Mater. Phys.* **2005**, *72*, 035455.

(59) Fogler, M. M. *Phys. Rev. Lett.* **2005**, *94*, 056405.

(60) Kané, G.; Lazzeri, M.; Mauri, F. *Phys. Rev. B: Condens. Matter Mater. Phys.* **2012**, *86*, 155433.

(61) Deshpande, V. V.; Chandra, B.; Caldwell, R.; Novikov, D. S.; Hone, J.; Bockrath, M. *Science* **2009**, *323*, 106.

(62) Bushmaker, A. W.; Deshpande, V. V.; Hsieh, S.; Bockrath, M. W.; Cronin, S. B. *Nano Lett.* **2009**, *9*, 2862.

(63) Katzenmeyer, A. M.; Léonard, F.; Talin, A. A.; Wong, P.-S.; Huffaker, D. L. *Nano Lett.* **2010**, *10*, 4935.

(64) Yu, Y.-J.; Zhao, Y.; Ryu, S.; Brus, L. E.; Kim, K. S.; Kim, P. *Nano Lett.* **2009**, *9*, 3430.

(65) Young, A. F.; Kim, P. *Nat. Phys.* **2009**, *5*, 222.